Tracing 2D Growth of Pancreatic Tumoroids Using the Combination of Image Processing Techniques and Mini-Opto Tomography Imaging System

Cihat Ediz Akbaba, MSc[1], Adem Polat, PhD[2] iD,
and Dilek Göktürk, PhD[3]

Abstract

Objectives: In this study, we aimed to trace the 2D growth development of tumoroids produced with MIA PaCa-2 pancreatic cancer cells at different time points. **Methods:** We cultured 3 different tumoroids with 0.5%, 0.8%, and 1.5% agarose concentrations and calculated the growth rate of the tumoroids with their images acquired at 9 imaging time points by mini-Opto tomography imaging system applying image processing techniques. We used the metrics contrast-to-noise ratio (CNR), peak signal-to-noise ratio (PSNR), and mean squared error (MSE) to analyze the distinguishability of the tumoroid structure from its surroundings, quantitatively. Additionally, we calculated the increase of the radius, the perimeter, and the area of 3 tumoroids over a time period. **Results:** In the quantitative assessment, the bilateral and Gaussian filters gave the highest CNR values (ie, Gaussian filter: at each of 9 imaging time points in range of 1.715 to 15.142 for image set-1). The median filter gave the highest values in PSNR in the range of 43.108 to 47.904 for image set-2 and gave the lowest values in MSE in the range of 0.604 to 2.599 for image set-3. The areas of tumoroids with 0.5%, 0.8%, and 1.5% agarose concentrations were 1.014 mm^2, 1.047 mm^2, and 0.530 mm^2 in the imaging time point-1 and 33.535 mm^2, 4.538 mm^2, and 2.017 mm^2 in the imaging time point-9. The tumoroids with 0.5%, 0.8%, and 1.5% agarose concentrations grew up to times of 33.07, 4.33, and 3.80 in area size over this period, respectively. **Conclusions:** The growth rate and the widest borders of the different tumoroids in a time interval could be detected automatically and successfully. This study that combines the image processing techniques with mini-Opto tomography imaging system ensured significant results in observing the tumoroid's growth rate and enlarging border over time, which is very critical to provide an emerging methodology *in vitro* cancer studies.

Keywords

cancer cells, image processing techniques, image segmentation, pancreatic cancer, tumoroid, tumors, MIA PaCa-2 cells, mini-Opto tomography

Abbreviations

ART, algebraic reconstruction technique; CAD, computer-aided design; CNR, contrast-to-noise ratio; DMEM, Dulbecco's Modified Eagle Medium; FBS, fetal bovine serum; MSE, mean squared error; PSNR, peak signal-to-noise ratio; ROI, region of interest; RGB, red-green-blue; 2D, two-dimensional; 3D, three-dimensional

[1] Department of Electrical and Electronics Engineering, Adana Alparslan Türkeş Science and Technology University, Adana, Türkiye
[2] Department of Electrical and Electronics Engineering, Çanakkale Onsekiz Mart University, Çanakkale, Türkiye
[3] Department of Bioengineering, Adana Alparslan Türkeş Science and Technology University, Adana, Türkiye

Corresponding Author:
Adem Polat, PhD, Department of Electrical and Electronics Engineering, Çanakkale Onsekiz Mart University, Çanakkale 17100, Türkiye.
Email: adempolat@comu.edu.tr

Correction (July 2023): The article type has been updated.

Introduction

Pancreatic cancer, one of the devastating cancer types, has no effective treatment for most patients. It is a highly malignant tumor that accounts for 216 000 new instances of cancer each year and results in 200 000 fatalities globally. Pancreatic cancer patients have a less than 5% 5-year survival probability because the disease metastasizes quickly to local lymph nodes and spreads hematogenously to distant organs. Surgery is the only possibly effective cure for pancreatic cancer.[1–6] The biology of pancreatic cancer, which is such a deadly disease, needs to be well understood to develop new treatment strategies, and it is predicted that it can be combated with personalized treatments in the future. For the development of individualized treatment plans, medication testing, and a deeper understanding of tumor biology, experimental systems are required. Cell cultures are considered excellent preclinical testing platforms.[7]

Most studies on the biology of cancer rely on *in vitro*, and two-dimensional (2D) cell culture techniques. The disruption of interactions between the cellular and extracellular environments, changes in cell shape, polarity, and mechanism of division are just a few of the drawbacks of 2D cultures. Due to these drawbacks, models that are better able to replicate *in vivo* circumstances have been developed. Culture using three-dimensional (3D) matrices to construct 3D tumoroids is one such approach.[8] In tumoroids, gradients occur in oxygen, nutrients, waste products, etc In addition, it is widely accepted that 3D cell–cell interactions alter cell signaling in response to soluble substances, which has a significant impact on cell function.[9]

The visualization of cancer cell spheroids has been studied with the research of various imaging techniques which has the potential to monitor drug carrier transportation to cancer cells in real-time using multicolor fluorescence microscopy.[10] In our previous studies, we proposed the cost-effective and portable mini-Opto tomography that enables 2D and 3D imaging of spheroids in a certain time interval for visualization.[4,11] Since microscopes cannot view biological samples with a size of a few cm in a single-window image, these samples can be viewed locally by moving them. From this perspective, it has been suggested that the mini-Opto tomography platform would be useful to researchers who want to observe how an entire tumor spheroid grown *in vitro* in cell culture develops within weeks.

One of the matrices, which is used for producing tumoroids, is agarose, a natural, biodegradable, nonadhesive, and nontoxic polymer obtained from seaweed. Agarose possesses the property required for building tumoroids, including high porosity (average pore size, 100-300 nm), which enables the replacement of nutritional media for 3D cell development and offers access to gases and small molecules. Also, agarose is an optically transparent substance that works well for microscopic spheroid viewing.[12] For these reasons, in our study, a pancreatic cancer tumoroid was created using the MIA PaCa-2 cell line, which is widely used *in vitro* studies of pancreatic cancer,[13,14] and agarose gel-based matrix.

Using computer-aided diagnosis (CAD) is the most effective way to diagnose cancer.[15] The CAD has recently been used to help doctors identify and locate suspicious cells in organs.[16] In order to develop effective treatment methods against cancer, appropriate observation and accurate analysis of cancer cells play an important role in developing effective treatment. The development of accurate diagnostic methods for cancer relies on meticulous tracing of the proliferation characteristics of cancerous cells that produce tumor mass in their natural medium. Segmentation of the tumor mass using computer-aided diagnoses is of great importance in quantitative and qualitative analysis of medical imaging.[17]

The cancerous structure used in this study was a tumoroid cultured with MIA PaCa-2 pancreatic cancer cells produced in a laboratory environment. The tumoroid was imaged with the mini-Opto tomography platform previously.[11] The mini-Opto tomography device is a cost-effective and portable imaging tool that enables 3D imaging of various biological specimens such as cancer cells. With this platform, a new 3D volumetric image is created by reconstructing 2D images of cancer cells obtained from different angles.[11] The algebraic reconstruction technique (ART) is one of the most frequently used reconstruction techniques and, with ART, a 3D image of a tumor can be reconstructed from the 2D projections of that tumor.[18] In this study, we cultured 3 tumoroids with MIA PaCa-2 pancreatic cancer cells in matrices with agarose concentrations of 0.5%, 0.8%, and 1.5%. We traced the growth developments of these 3 tumoroids at 9 imaging time points (a total of 27 images) with 2D images obtained via the mini-Opto tomography platform using the property of zero-degree angle imaging of it.

Materials and Methods

Many computer software and image processing libraries are available to detect cancer cells from images by applying image processing techniques.[19,20] In our study, the Python programming language and OpenCV library were used to perform image processing techniques on the images of the tumoroid. With the mini-Opto tomography imaging system, 2D images of 3 different tumoroid cultures with 0.5%, 0.8%, and 1.5% agarose concentration were taken at 9 imaging time points for each, and 3 different image sets were obtained. These 3 image sets were imported by Python programming environment which is an open-source software to be processed through a series of steps. Additionally, the OpenCV library which is an open-source library used for image and video analysis created by INTEL was used for image processing methods.[21] We worked with the OpenCV library of the Python programming language which consists of 2 main parts (preprocessing and segmentation) for thresholding (ie, threshold values of wide range), morphological operations (ie, 3×3-15×15 kernels for erosion and dilation), contour calculations (detecting and drawing the borders of tumoroids), and feature extraction (ie, perimeter, diameter, and area).

The preprocessing consists of uploading images, region of interest (ROI), red-green-blue (RGB) to gray transformation and filtering steps. The segmentation section consists of thresholding,
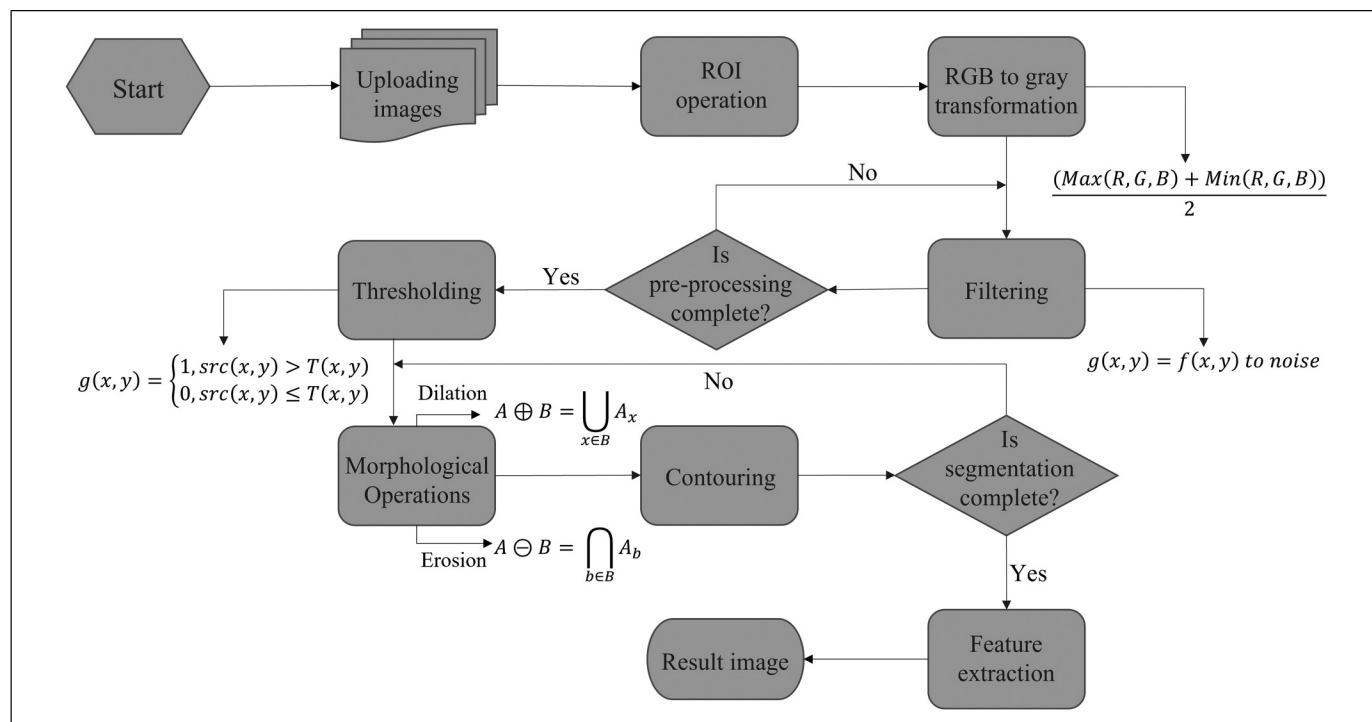
Figure 1. The flowchart of image processing, segmentation, and feature extraction steps for the tumoroid images. A total of 6 processes were performed to distinguish tumoroids where they were located. These processes were ROI operation, RGB to gray transformation, filtering, thresholding, morphological operations, and contouring. After the images' preprocessing and segmentation, the tumoroid images' features were extracted in the feature extraction step.
Abbreviations: ROI, region of interest; RGB, red-green-blue.

morphological operations, and contour area-perimeter-radius calculation steps. These steps are shown in Figure 1.

Cell Culture Preparation

Preparation of pancreatic cancer cell culture. Human pancreatic cancer cell line MIA PaCa-2 (ATCC® CRL-1420TM) was cultured (Figure 2a) using 10% fetal bovine serum (FBS)-supplemented Dulbecco's Modified Eagle Medium (DMEM) without antibiotics in a humidified incubator at 37 °C and 5% CO_2 atmosphere. After approximately 70% confluence, cells were passaged, and the culture media was switched every 2 days.[4]

Preparation of tumoroids. The agarose gel-based matrices utilized in this study to create MIA PaCa-2 pancreatic tumoroids. 2.5 mL of 0.5%, 0.8%, and 1.5% agarose solutions were prepared and heated in a microwave, and they were put into 33 mm diameter Petri dishes for cell culture and allowed to polymerize. After that, each Petri dish received 2.5 mL of the culture medium (DMEM + 10% FBS) and was maintained for 1 day at 37 °C.

A total of 100 cells in 10 μL volumes were pipetted into the dishes, it was allowed to absorb the solution by the agarose matrices for 2 h, then a cell culture medium was added to the cells and the Petri dishes were placed in the incubator with their bottoms facing up. Standard incubation conditions were used for the cultures (5% CO_2, 37 °C). The culture media were replaced 4 days after the initial seeding, and this process was repeated every 2 days after that. The plates were removed from the incubator every 2 days to observe the development of tumoroids with an inverted phase contrast microscope (Leica, Dmil Led Fluo). The imaging of 3 tumoroid cultures with 0.5%, 0.8%, and 1.5% concentrations was initiated with the mini-Opto tomography imaging system (Figure 2b, c) after observing the effective formation and proper growth of the tumoroid by the inverted phase contrast microscope (Figure 2a).

Image acquisition. The images of 3 different sets were acquired via mini-Opto tomography imaging system (Figure 2b, c) that is capable of angular imaging from different angles (e.g., −/+45-degree) of the sample.[4,11] In this study, we only operated the 2D imaging characteristic of mini-Opto tomography imaging system using the zero-degree angle scanning operation on different days (9 different imaging time points) to observe the size change of the 3 different tumoroids over time. The image set-1, the image set-2, and the image set-3 were created for tumoroids prepared by 0.5%, 0.8%, and 1.5% agarose concentrations, respectively.

Image preprocessing. The images obtained from the mini-Opto tomography imaging system were RGB images. In this study,
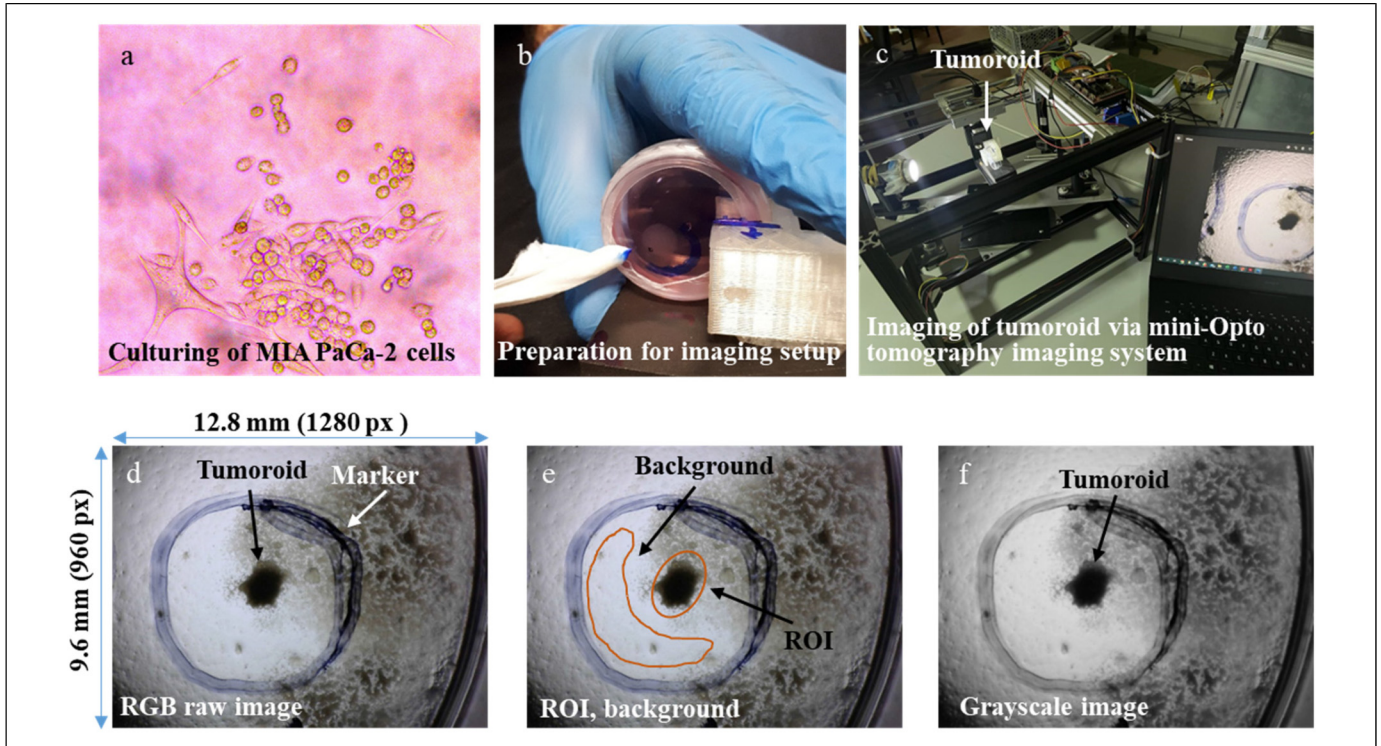
Figure 2. Tumoroid culture and imaging experiment setup. (a) First image was taken with the inverted phase contrast microscope after culturing MIA PaCa-2 pancreatic cancer cells. (b) Preparation for imaging setup, that is, marking the surrounding tumoroid with a marker. (c) Placement of Petri dish that includes tumoroid into the mini-Opto tomography imaging system. (d) RGB raw image with the size of 9.6 mm × 12.8 mm (resolution: 960 pixels × 1280 pixels) acquired by the mini-Opto tomography imaging system. (e) Selecting ROI and background to determine the distinguishability of the tumoroid from the medium where it is located. (f) Converting the raw image to a grayscale image for use in the preprocessing step.
Abbreviations: ROI, region of interest; RGB, red-green-blue.

since the RGB color channel image contains more structural information than the single channel grayscale image, only grayscale images consisting of grayscales ranging from the weakest intensity black to the strongest white intensity were used.[22–24] We converted the images from RGB to grayscale format by applying equation (1) to perform the next steps of image processing such as filtering, thresholding, morphological operations, and contour-area calculation (Figure 1) in our implementation.

$$RGBtoGray = (Max(R, G, B) + Min(R, G, B)) / 2 \quad (1)$$

where $Max(R, G, B)$ and $Min(R, G, B)$ are the maximum and minimum values of the range of 0 to 255 intensity value of each R, G, and B, respectively. $RGBtoGray$ is the average value of the most prominent and least prominent colors.

In order to distinguish the tumoroid borders from the environment where they are located, it is necessary to perform preprocessing on the images. The preprocessing step consists of uploading images, ROI operation, RGB to grayscale transformation, and image filtering.

In the first step, the raw format of RGB images (Figure 2d) was loaded into the ImageJ program to determine the ROI and background of ROI. Then, the ROI and background of ROI were selected manually on the raw images, allowing the

human eye to distinguish the cancerous region (tumoroid borders) from its surrounding (Figure 2e). The raw format of RGB images (Figure 2d) was also uploaded into the Python program to convert it to the grayscale format (Figure 2f) in the preprocessing step.

In the second step, the raw format of RGB images (Figure 2d) was converted to grayscale (Figure 2f) to apply various image filtering methods and to perform image segmentation. The effect of the filters applied to the images on the evaluation of image quality during the preprocessing stage is crucial for the segmentation step. Because the rate of distinguishing the tumoroid from the image background at the image segmentation stage is directly related to the processes to be performed for noise removal at the preprocessing stage before segmentation.

There were some disorders at the boundaries of tumoroid and noises on image sets with grayscales. By applying filtering operation on the images to obtain enhanced images, the disorders were smoothed, and the noises were removed. To increase the appearance details of the tumoroid mass, we applied to mean, median, bilateral, and Gaussian filters, respectively. Additionally, we applied different sizes of core matrices (kernel) such as 5 × 5 for the median filter and 3 × 3 for the bilateral filter to the input images.

In order to explain the filtering concept in general and the mathematical operation behind it, bilateral filtering, one of the
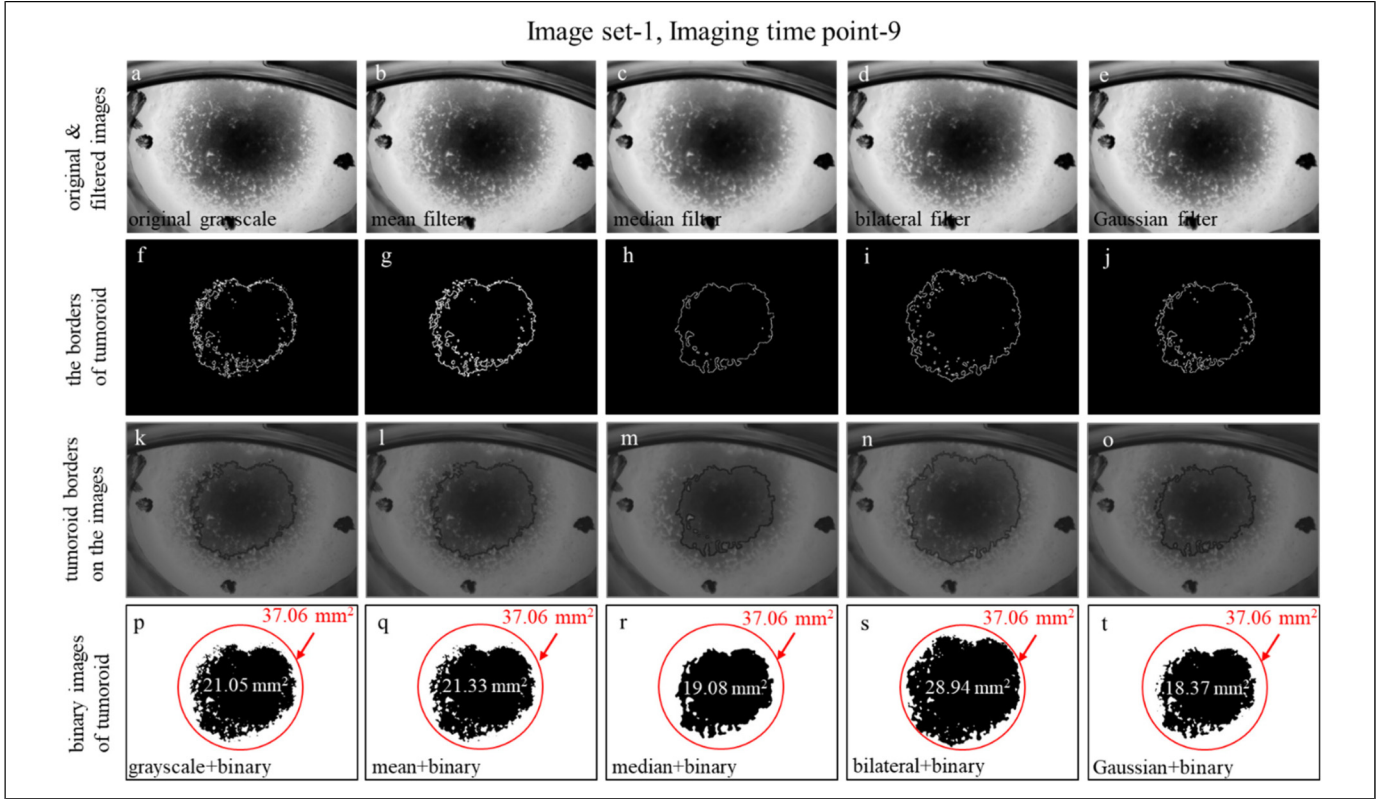
Figure 3. Preprocessing of images. (a) Original grayscale image. (b–e) Filtered images were obtained after applying mean, median, bilateral, and Gaussian filters to the grayscale image. (f–j) Obtaining the borders of filtered images with Sobel edge detection. (k–o) Blended images combined with grayscale-filtered images and bordered images. (p–t) After thresholding to the grayscale-filtered images, tumoroid areas of grayscale-filtered images and area of the minimum surrounding circle of the tumoroid.

filtering methods applied in the study, is discussed in this section. The bilateral filter introduced by Tomasi and Manduchi in 1988 is a nonlinear technique that uses the Gaussian kernel in spatial space and density.[25] The bilateral filter is one of the most effective filters for removing noise while protecting edges. In this method, geometrical distances and gray-level similarities of the surrounding pixels are taken into consideration. The bilateral filter takes the sum of the weights of the pixel values in a local neighborhood. This weight can vary depending on both the spatial distance and the density distance of the pixel value.[26] The bilateral filter is expressed as follows:[27,28]

$$I^{filtered}(x) = \frac{1}{W_p} \sum_{x_i \in \Omega} I(x_i) f_r(||I(x_i) - I(x)||) g_s(||x_i - x||) \quad (2)$$

$$W_p = \sum_{x_i \in \Omega} f_r(||I(x_i) - I(x)||) g_s(||x_i - x||) \quad (3)$$

where $I^{filtered}$ is the filtered image, x_i is a pixel in a given input image window, and $I(x_i)$ is the intensity at the current pixel. x is the coordinates for the current pixels for filtered images, Ω is the window centered in x_i, f_r is the kernel size to smooth differences in intensities, g_s is the spatial kernel to smooth differences in coordinates, and W_p is the normalization term.

We applied individually these 4 filtering methods to each 9 imaging time points of 3 image sets for comparing the result performances. Figure 3 shows an example of the comparison of mean-filtered, median-filtered, bilateral-filtered, and Gaussian-filtered images (Figure 3a-e) for the imaging time point-9 in the image set-1. We utilized a Sobel edge detector to highlight sharp changes in intensity in the images using the ImageJ program. The Sobel edge detector[29] provided the borders of the tumoroids in original grayscale, mean-filtered, median-filtered, bilateral-filtered, and Gaussian-filtered images (Figure 3f-j). The borders were masked onto the images to compare the effects of the various filter types (Figure 3k-o). We converted the original and filtered images to the binary format to observe the dissimilarities of tumoroid borders (details are explained in Image Segmentation section) in each image (Figure 3p-t). We created a reference circle (in red color in Figure 3p-t) that has a minimum radius fully covering the tumoroid binary image obtained by the bilateral filter which has a maximum area to compare the areas calculated by a variety of filter applications. We calculated the areas of tumoroid (details are explained in Feature Extraction section) as 21.05 mm², 21.33 mm², 19.08 mm², 28.94 mm², and 18.37 mm² for original grayscale, mean-filtered, median-filtered, bilateral-filtered, and Gaussian-filtered images, respectively (Figure 3p-t). The maximum area of the tumoroid was obtained in the bilateral

filter application (Figure 3d, i, n, s). Referring to this assessment, in Results and Discussion section, we comprehensively presented Table 2, which shows the total areas of tumoroids (details are explained below), and Figure 7, which includes the tumoroid borders of binary images at a total of 27 imaging time points of the 3 image sets.

Since the raw and filtered images appear close to each other to the naked eye as seen in Figure 3, we evaluated the performance of the filter methods quantitatively. To distinguish the tumoroid mass from its surrounding, various metrics such as the contrast-to-noise ratio (CNR), peak-to-signal noise ratio (PSNR), and mean squared error (MSE) were calculated for the images to be able to measure the efficiency of filters and to evaluate the quantitative analysis.

We used the CNR metric to determine which filter was more effective in separating the tumoroid mass in the images. CNR is a quantitative measure used to determine how clearly the object of interest in an image can be distinguished from the image background. The *CNR* formula we calculated on the images is given in equation (4).[30]

$$CNR = \frac{\mu_{ROI} - \mu_{BACKGROUND}}{\sigma_{BACKGROUND}} \qquad (4)$$

Looking at equation (4), μ_{ROI}, $\mu_{BACKGROUND}$, and $\sigma_{BACKGROUND}$ are the mean value of ROI, the mean value of the background of ROI, and the standard deviation of the background, respectively.

Another metric used to measure the performance of the filters was *PSNR*, and is calculated as follows:[31]

$$PSNR = 10 \log \frac{255^2}{MSE} \qquad (5)$$

In equation (5), 255 is the maximum value representing the 8-bit gray level, and the *MSE* is the value that measures the mean square difference between the actual and ideal pixel values. High value in the calculation used to measure the quality between the original image and the output image means that the quality of the image obtained is high.[32,33]

MSE is a metric that is usually used to measure the similarities of 2 images, and a low result of *MSE* means that the similarity in the image is high.[34] *MSE* value is calculated as follows:

$$MSE = \frac{1}{MN} \sum_{j=1}^{M} \sum_{i=1}^{N} (G(i,j) - F(i,j))^2 \qquad (6)$$

In equation (6), the *M* and *N* values are the total number of pixels in the column and row of the image. *G* value represents the original noisy image, *F* value represents the filtered image.[35]

Image segmentation. In the segmentation section of the image processing technique, the desired and/or target region in an image is separated from its surrounding area by applying various operations. In our study, the main goal of the segmentation process is to distinguish the main structure of the tumoroid in the growth medium by eliminating artifacts outside of the tumoroid. The tumoroid was initially separated from the

background by applying segmentation steps consisting of thresholding, morphological, and contouring operations. In the thresholding method, which is an important step in image processing, in order to separate the target object from the image in its environment, a segmentation is made between the target region and the background by selecting the appropriate threshold values.[24] In this study, threshold operation was performed on the filtered images and the area of tumoroid was detected by sharpening boundaries in the culture environment where the MIA PaCa-2 cells were grown.

For performing the segmentation between the tumoroid mass and its background, the binary threshold function returns to 0 or 1 and that is expressed in equation (7). Since the difference between the object and the background is obvious, the global thresholding method, which is one of the thresholding methods,[36] was used in our study to separate the tumoroid (object) from the background. The binary threshold function that is used for the global thresholding method has 4 parameters which are the grayscale source image, the threshold value classifying pixel values, the maximum value, and the threshold type, respectively.

$$g(x,y) = \begin{cases} 1, & src(x,y) > T(x,y) \\ 0, & src(x,y) \leq T(x,y) \end{cases} \qquad (7)$$

where the value of $src(x,y)$ is the pixel value of each source image, $T(x,y)$ is the selected threshold pixel value, and $g(x,y)$ is the obtained pixel value of the image after applying the thresholding operation. Here, if the value of $src(x,y)$ is greater than $T(x,y)$, the pixel value of the resulting image would be 1 otherwise, the pixel value would be 0. According to the values of 0 and 1, pixels in the image is divided into 2 groups perfectly black and white.

In the Image Segmentation section, another important step is the morphological operation which is used to reduce structural distortions in certain parts of an image[37] and explained next part of the article. With this operation, it was eliminated the regions that are the nontumoroid and artifacts to obtain ROI, which is tumoroid in all image sets.

As morphological operations on an image, dilation, erosion, opening and closing methods are performed for various purposes. Using morphological image processing, the elimination of unwanted objects is possible with different combinations of dilation and erosion.[38] In our study, we preferred dilation which provides the objects in the images to expand and erosion which provides thinning of the objects in the image[39] to apply to the binary image.

For the whole imaging time points of the 3 image sets we used in our study, morphological processes with different kernel sizes were applied to distinguish the tumoroid structures in the images clearly. In the OpenCV environment, the dilate function ($\oplus$ in equation (8)) that performs the dilation operation takes 3 parameters that consist of the source image, the kernel which is a set of a pixel that expand the source image, and iterations. By defining that A is a source image and B is a small pixel set, the dilation process is expressed by the following

formula, where the A_x is the translation of A by B, that is, each value of the array set A is shifted by B.[40]

$$A \oplus B = \bigcup_{x \in B} A_x \qquad (8)$$

The erosion operation is expressed by Minkowski subtraction by the following erosion function ($\ominus$ in equation (9)) formula where A_b is the translation of A by b.[40]

$$A \ominus B = \bigcap_{b \in B} A_b \qquad (9)$$

The set of B pixels is moved over A to perform erosion. If all of the pixel values of B overlap with A, that is, it is covered by A, the pixels of the array A corresponding to the center of B are preserved. Otherwise, pixels including B in the set of A array are converted to the background pixels of A.

It is recommended to create the opening and closing morphological operations by combining dilation and erosion operations in case dilation and erosion are not sufficient separately to evaluate the ROI region in accordance with its purpose. Opening and closing operations are used for implementations such as noise removal, object simplification, and hole filling[41] to obtain the main structure by filling and/or removing related but disconnected areas. In the opening process, first erosion is performed followed by dilation whereas the opposite of the opening process is done in the closing process. The opening ($\circ$) and the closing ($\bullet$) operations are defined in equations (10) and (11), respectively.

$$A \circ B = (A \ominus B) \oplus B \qquad (10)$$

$$A \bullet B = (A \oplus B) \ominus B \qquad (11)$$

To understand the effects of dilation, erosion, opening, and closing processes for an image, we presented the results of these operations taking an example of the imaging time point-6 of image set-2, which are shown in Figure 4c-f, respectively. After determining the ROI borders in the gray format (Figure 4a) of the original image, we observed the surplus regions that remain outside the ROI, which may be assumed as tumoroid in the binary transformation (Figure 4b). However, excessive selection of ROI boundaries may also cause nontumoroid regions to be misdiagnosed as the tumoroid structure (Figure 4b). To make a deep evaluation of whether the selected ROI fits the tumoroid in the image completely, the effects of dilation, erosion, opening, and closing operations (Figure 4d-f) were taken into consideration and interpreted. Although the detached and lighter areas around the dark black area were also part of the tumoroid, they were assumed to be invading parts and therefore excluded from the tumoroid. According to the selected ROI in Figure 4a, the results obtained by the dilation (Figure 4c) and opening (Figure 4e) operations were closer to the tumoroid compared to the results obtained by the binary (Figure 4b), erosion (Figure 4d), and closing (Figure 4f) operations in the qualitative evaluation.
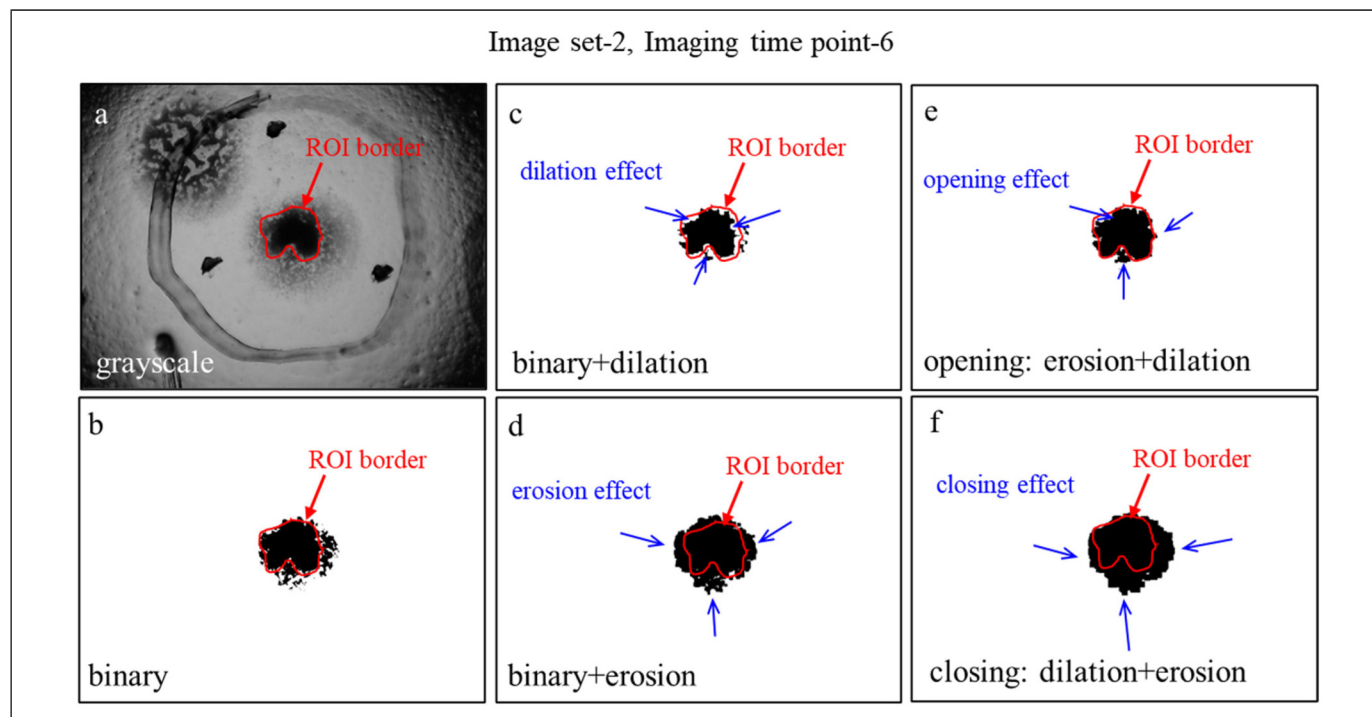

Figure 4. Morphological operations. (a) Region of interest (ROI) border of the tumoroid in the grayscale image. (b) Applying binarization to the grayscale image. (c–f) Effects of dilation, erosion, opening and closing operations on the binary image, respectively.

Another important step in the segmentation stage is contour drawing which is the joint of pixels along the boundaries of the ROI[42] to obtain a specified object that is a tumoroid in our study. In our study, the x and y coordinates of the relevant tumoroid structures were calculated and the contours surrounding the tumoroid were drawn on the original images by combining continuous points with the same density. The pseudocode of the contouring process in segmentation is presented below.

```
-Segmentation
-Thresholding
-Morphological operations
-Contouring
 -finding contours of each eroded/dilated images
   >>for i = each image, importing images[i]
     >>find all contours* of image[i]
           Parameters (source image, contour retrieval
                 mode, contour approximation method)
     >>draw all contours** of image[i]
           Parameters (source image, contour retrieval
                 mode, contour approximation method)
     >>delete of the contours except tumoroid's contour
     >>overlay the contours on the original RGB image.
   >>end
```

* Each individual contour is a Numpy array of (x, y) coordinates of boundary pixels that have the same color and intensity of the tumoroid.

** Select the coordinate points of the contour to draw the contour lines of the tumoroid.

In the study, filtered-binary images were used, and the contours of the ROIs were automatically and successfully detected for distinguishing the largest borders of the tumoroid in the 3 image sets.

Feature extraction. Feature extraction is one of the most important phases in detecting cancer at an early stage.[43] We extracted various image features from pancreatic cancer (MIA PaCa-2 cells) images by applying preprocessing and segmentation steps for 3 image sets. We calculated the area, perimeter, and radius features at each of 9 different imaging time points of 3 image sets to observe the development of tumoroid growth.

We presented Figure 5 to illustrate how we determined the contour, area, perimeter, and diameter of the tumoroid for 3 sets of images, citing the imaging time point-9 in image set-3 as an example. In the contouring operation, tumoroid contour (in green color in Figure 5a) was drawn automatically surrounding the tumoroid in the original images (Figure 5a). A reference circle (in blue color in Figure 5b and c) that has a minimum diameter fully covering the tumoroid was created (Figure 5b and c). We calculated the area, perimeter, and diameter of tumoroid as 1.984 mm^2, 6.018 mm, and 1.880 mm, respectively (Figure 5a–c). We illustrated the binarization formats of tumoroid border, contoured tumoroid border, and minimum diameter surrounding the tumoroid border in Figure 5d–f, respectively. To emphasize the effects of filtering methods,

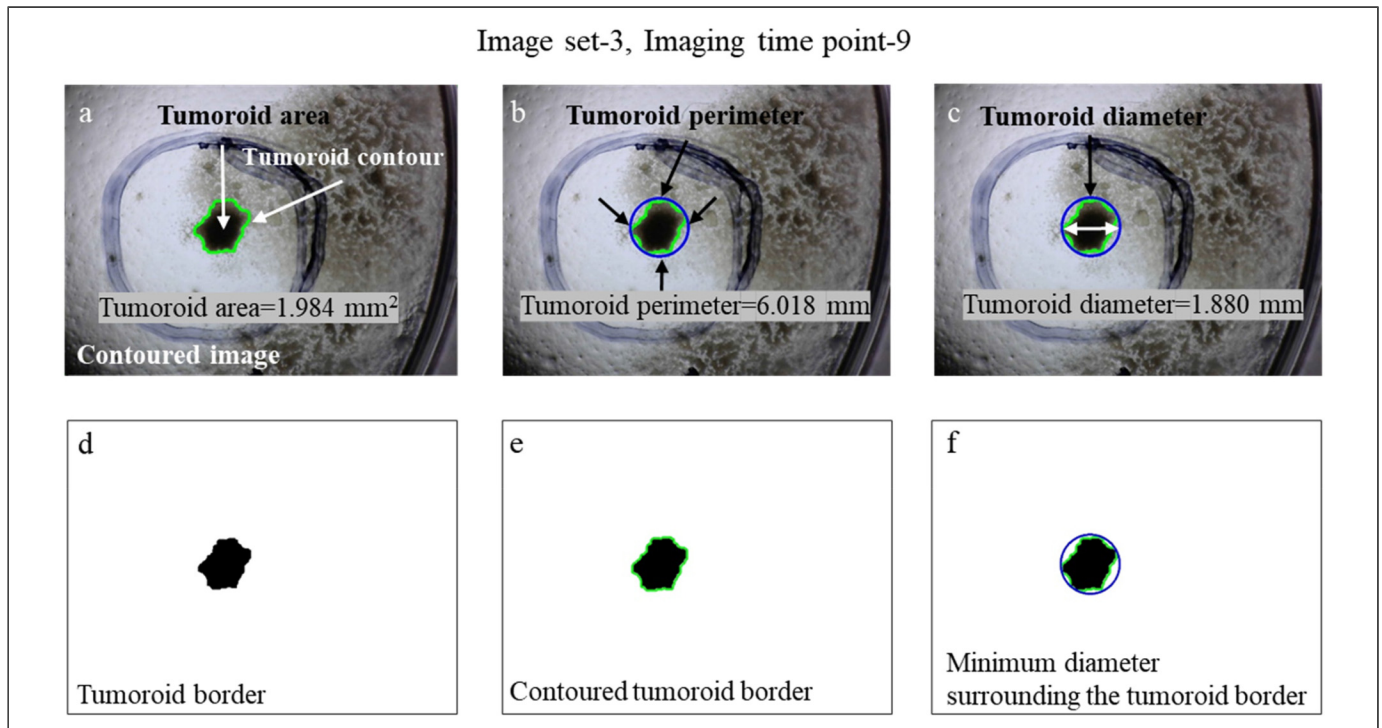**Figure 5.** Feature extractions of the 3 image sets, that is, Image set-3, Imaging time point-9. (a) Contouring and calculating the area of tumoroid, that is, tumoroid area of image set-3 at imaging time point-9 was 1.984 mm^2. (b) The perimeter of tumoroid was 6.018 mm. (c) The diameter of tumoroid was 1.880 mm. (d–f) Binary formats of tumoroid border, contoured tumoroid border, and minimum diameter surrounding the tumoroid border.

binarization, morphological operations, and contouring we presented some results in Figure 3, Figure 4, and Figure 5 just to make it clear how material and methods work in this concept.

Results

The 3 sets of images used for the proposed image processing techniques were obtained with zero angles from the mini-Opto tomography device at 9 different imaging time points. We analyzed the results by applying the stages of pre-processing and segmentation such as filtering, binarization, morphological process, contouring, and feature extraction for each imaging time point of the 3 image sets. We evaluated the outcomes of all processing for all data qualitatively and quantitatively.

In quantitative evaluation (Table 1), the median filter gave the highest values in PSNR measurement in the range of 46.656 to 57.675, 43.108 to 47.904, and 43.989 to 50.316, and gave the lowest values in MSE measurement in the range of 0.111 to 1.404, 1.053 to 3.178, and 0.604 to 2.599 for image sets-1, 2, and 3, respectively. Additionally, the CNR values of median filtered images were in the range of 1.714 to 14.120, 10.750 to 41.058, and 11.886 to 44.742, for image sets-1, 2, and 3, respectively. However, although the PSNR and MSE values of median filtered images were the highest and lowest among the filter methods, the CNR values of median filtered images were not superior results as expected. The bilateral and Gaussian filters gave the highest CNR values compared to the CNR values of median-filtered images because the median filter caused smoother images and smoothing produced lower CNR values. For instance, the CNR values of bilateral filtered images were in the range of 1.715 to 15.216, 10.788 to 41.947, and 16.642 to 45.460 for image sets-1, 2, and 3, respectively.

Figure 6 shows the compared outcomes of the binarization, morphological operations, contouring, and feature extraction for image sets-1, 2, and 3 at imaging time point-5 as an example.

After binarization, morphological operations were applied to fill the intra-tumoroid spaces and eliminate nontumoroid structures, and the contours of the tumoroids borders were drawn. Finally, the radius, the perimeter, and the area calculations, which are the image features, were made by drawing the reference circles fully surrounding the tumoroids. According to these results, at imaging time point-5 for image sets-1, 2, 3; the radius of 1.590 mm, 0.940 mm, 0.730 mm; the perimeter of 12.035 mm, 7.090 mm, 4.575 mm; and the area of 6.497 mm^2, 1.964 mm^2, 1.390 mm^2, respectively. These results showed that the area of tumoroid produced by agarose gel 0.5% (image set-1) was approximately 3.3 times the one produced by agarose gel 0.8% (image set-2) and 4.67 times the one produced by agarose gel 1.5% (image set-3). This showed the importance of the effect of agarose concentration on tumoroid growth.

To trace the evolution of tumoroid produced with MIA PaCa-2 cells at various stages of 2D growth, for image sets-1, 2, and 3 with 0.5%, 0.8%, and 1.5% agarose concentration, respectively; in Figure 7, we presented the original, contoured, binary-bordered versions of the tumoroid images acquired at 9 imaging time points.

As can be seen from Figure 7, in qualitative assessment, the tumoroid with 0.5% agarose concentration given 2D images with image set-1 showed a much faster growth trend in the same time period than tumoroid with 0.8% and 1.5% agarose concentration. In the quantitative assessment as shown in Table 2, the tumoroid with 0.5% agarose concentration (image set-1) showed a 33.07 times growth increasing from 1.014 mm^2 at imaging time point-1 to 33.535 mm^2 at imaging time point-9. Likewise, the tumoroid with 0.8% agarose concentration (image set-2) grew up 4.33 times increasing from 1.047 mm^2 at imaging time point-1 to 4.538 mm^2 at imaging time point-9; the tumoroid with 1.5% agarose concentration (image set-3) showed a 3.80 times growth, increasing from 0.530 mm^2 at imaging time point-1 to 2.017 mm^2 at imaging time point-9. This shows that the tumoroid prepared with low-concentrated agarose gel grows much faster and the rate of tumor growth and development decreases as the agarose concentration is increased. Similarly, the perimeter and the radius of the tumoroid with 0.5% agarose concentration (image set-1) increased rapidly from 4.758 mm to 33.569 mm (7.05 times) and from 0.670 mm to 3.680 mm (5.49 times), respectively. The perimeter and the radius of the tumoroid with 0.8% agarose concentration (image set-2) increased from 4.481 mm to 12.157 mm (2.71 times) and from 0.670 mm to 3.720 mm (2.27 times), respectively. The perimeter and the radius of the tumoroid with 1.5% agarose concentration (image set-3) increased from 2.913 mm to 6.018 mm (2.06 times) and from 0.670 mm to 3.720 (2.04 times) mm, respectively.

In Figure 8, we presented the growth trend of 3 tumoroids with 0.5%, 0.8%, and 1.5% agarose concentrations over time for easy comparison by visualizing the value changes of the area, perimeter, and radius.

Discussion

When the results of the study were evaluated and compared with similar studies in the literature, it was seen that there were some similarities and differences. In a study by Alhadidi et al.,[19] although the threshold method was applied to mammogram breast cancer images at the segmentation stage, the image was not clearly segmented. In our study, we applied the global thresholding method to the MIA PaCa-2 pancreatic cancer images obtained by mini-Opto tomography platform in the segmentation stage and achieved successful results in highlighting the tumoroid masses. In a study by Xie and Lu,[24] only the median filter method, which is a nonlinear smoothing technique, was used as a filter in the preprocessing stage to separate copper cores in the tiny wire. However, in our study, in the preprocessing stage, we used the mean, median, bilateral, and Gaussian filter methods comparing their performance in eliminating the noises on the images of tumoroid. In a study by

Table 1. PSNR, MSE, and CNR Values of the Mean-, Median-, Bilateral-, and Gaussian-Filtered Images for 3 Image Sets, Each of 9 Imaging Time Points.

		PSNR				MSE				CNR			
		Mean	Median	Bilateral	Gaussian	Mean	Median	Bilateral	Gaussian	Mean	Median	Bilateral	Gaussian
Image set-1	Imaging time point-1	52.479	57.675	52.125	53.414	0.367	0.111	0.398	0.296	1.714	1.714	1.715	1.715
	Imaging time point-2	45.778	53.347	45.44	46.557	1.718	0.300	1.856	1.436	3.575	3.568	3.576	3.573
	Imaging time point-3	45.801	53.376	45.445	46.470	1.709	0.298	1.855	1.465	2.476	2.475	2.477	2.476
	Imaging time point-4	47.360	54.357	46.890	48.194	1.193	0.238	1.330	0.985	15.171	14.120	15.216	15.142
	Imaging time point-5	46.506	54.5261	46.092	47.331	1.453	0.229	1.598	1.201	8.064	8.046	8.069	8.062
	Imaging time point-6	44.140	51.881	43.694	44.945	2.506	0.421	2.777	2.082	8.155	8.134	8.160	8.151
	Imaging time point-7	46.550	54.167	46.054	47.348	1.438	0.249	1.612	1.197	3.196	3.196	3.206	3.196
	Imaging time point-8	47.280	53.658	46.791	48.194	1.216	0.280	1.361	0.985	3.408	3.406	3.409	3.408
	Imaging time point-9	40.339	46.881	39.954	41.039	5.655	1.404	6.222	4.852	2.692	2.689	2.693	2.692
Image set-2	Imaging time point-1	42.974	47.904	42.705	43.504	3.278	1.053	3.487	2.901	31.907	31.644	31.944	31.866
	Imaging time point-2	42.291	46.931	42.038	42.851	3.836	1.318	4.066	3.372	41.833	41.058	41.947	41.716
	Imaging time point-3	41.545	46.254	41.241	42.083	4.555	1.540	4.885	4.025	17.833	17.645	17.863	17.818
	Imaging time point-4	41.584	46.551	41.235	42.196	4.514	1.438	4.892	3.920	21.874	21.676	21.922	21.851
	Imaging time point-5	41.409	46.603	41.034	42.030	4.700	1.421	5.123	4.074	14.387	14.363	14.389	14.387
	Imaging time point-6	40.387	45.661	39.999	41.028	5.947	1.765	6.503	5.131	18.563	18.394	18.596	18.533
	Imaging time point-7	39.115	44.352	38.733	39.824	7.971	2.386	8.704	6.769	10.785	10.750	10.788	10.779
	Imaging time point-8	39.513	44.744	39.131	40.229	7.273	2.180	7.941	6.168	15.093	14.927	15.124	15.071
	Imaging time point-9	38.116	43.108	37.754	38.764	10.372	3.063	11.268	8.980	13.663	13.409	13.717	13.636
Image set-3	Imaging time point-1	43.816	50.241	43.412	44.458	2.700	0.615	2.963	2.329	16.623	16.555	16.642	16.616
	Imaging time point-2	43.766	50.316	43.275	44.464	2.731	0.604	3.058	2.326	17.299	17.150	17.416	17.147
	Imaging time point-3	43.486	49.789	43.031	44.179	2.913	0.682	3.235	2.483	37.818	37.241	37.893	37.707
	Imaging time point-4	43.280	49.468	42.842	43.985	3.055	0.734	3.379	2.597	45.382	44.742	45.460	45.302
	Imaging time point-5	43.350	49.345	42.849	44.104	3.006	0.755	3.373	2.527	22.434	22.328	22.539	22.414
	Imaging time point-6	42.167	47.682	41.739	42.844	3.947	1.108	4.356	3.377	23.576	23.365	23.593	23.544
	Imaging time point-7	39.012	44.222	38.624	39.720	8.163	2.459	8.925	6.934	25.983	25.216	26.115	25.872
	Imaging time point-8	39.594	45.010	39.141	40.347	7.138	2.051	7.923	6.001	24.186	23.443	24.315	24.099
	Imaging time point-9	38.549	44.102	38.123	39.332	8.587	2.599	9.467	7.206	20.212	19.704	20.308	20.175

Abbreviations: CNR, contrast-to-noise ratio; MSE, mean-sqaured error; PSNR, peak signal-to-noise ratio.

Table 2. The Values of the Area in mm², Perimeter in mm, and Radius in mm for 9 Imaging Points of Image set-1, Image set-2, and Image set-3.

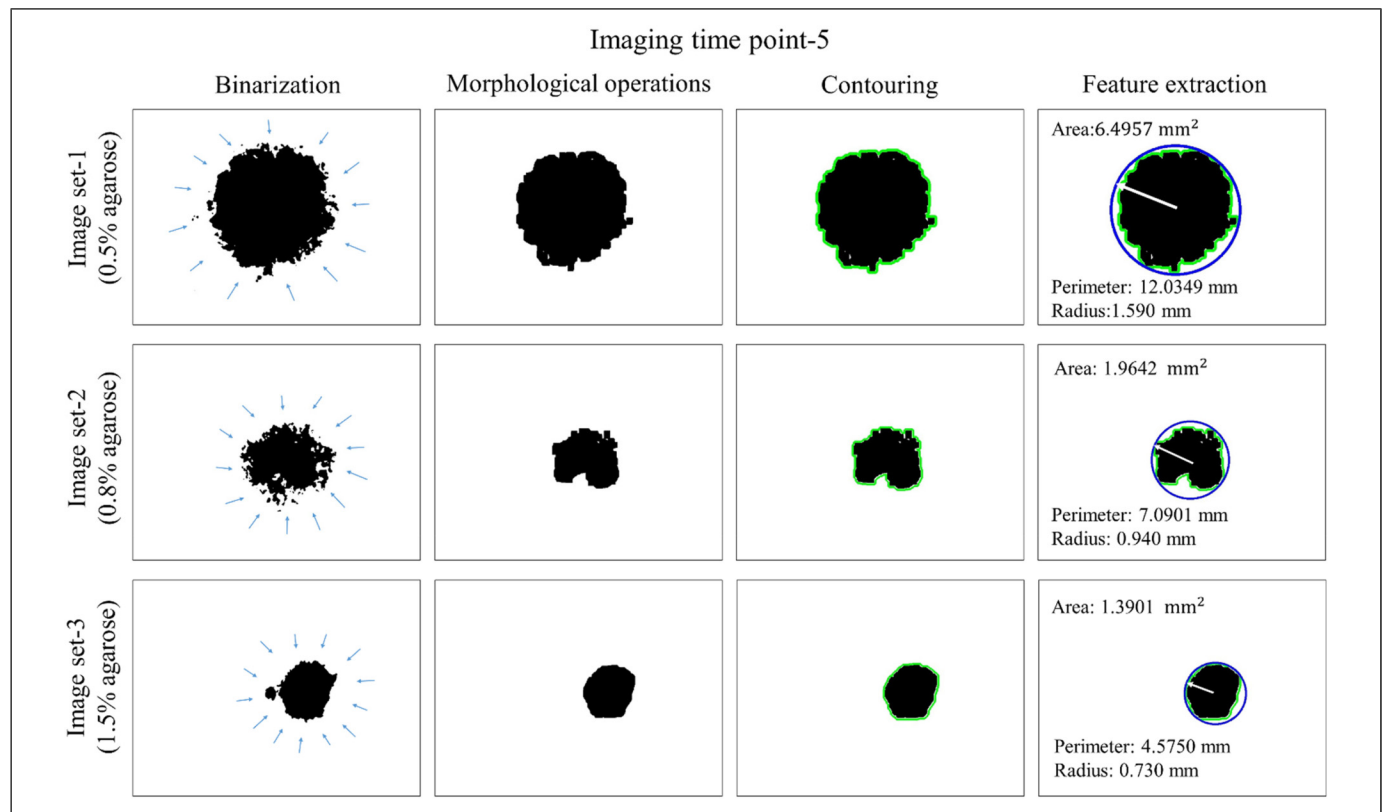|	Image set-1			Image set-2			Image set-3		
	Area (mm^2)	Perimeter (mm)	Radius (mm)	Area (mm^2)	Perimeter (mm)	Radius (mm)	Area (mm^2)	Perimeter (mm)	Radius (mm)
Imaging time point-1	1.014	4.758	0.670	1.047	4.481	0.700	0.530	2.913	0.460
Imaging time point-2	1.108	4.819	0.710	1.304	4.909	0.750	0.725	3.363	0.550
Imaging time point-3	1.184	4.894	0.720	1.603	6.196	0.900	1.025	3.933	0.650
Imaging time point-4	2.623	9.256	1.060	1.748	6.221	0.880	1.179	4.243	0.690
Imaging time point-5	6.495	12.034	1.590	1.964	7.090	0.940	1.390	4.575	0.730
Imaging time point-6	9.946	12.477	1.890	2.281	7.643	1.020	1.470	4.962	0.780
Imaging time point-7	19.576	23.936	2.740	2.559	7.665	1.080	1.617	5.531	0.840
Imaging time point-8	31.988	32.284	3.560	2.883	8.917	1.130	1.927	5.914	0.910
Imaging time point-9	33.535	33.569	3.680	4.538	12.157	1.590	2.017	6.018	0.940

Figure 6. Binarization, morphological operations, contouring, and feature extraction at imaging time point for image sets-1 (0.5 agarose), 2 (0.8 agarose), and 3 (1.5 agarose) at the first, second, and third rows, respectively. To illustrate that these calculations were made for all 27 imaging time points for 3 image sets, area, perimeter, and radius values for imaging time point-5 were given here.
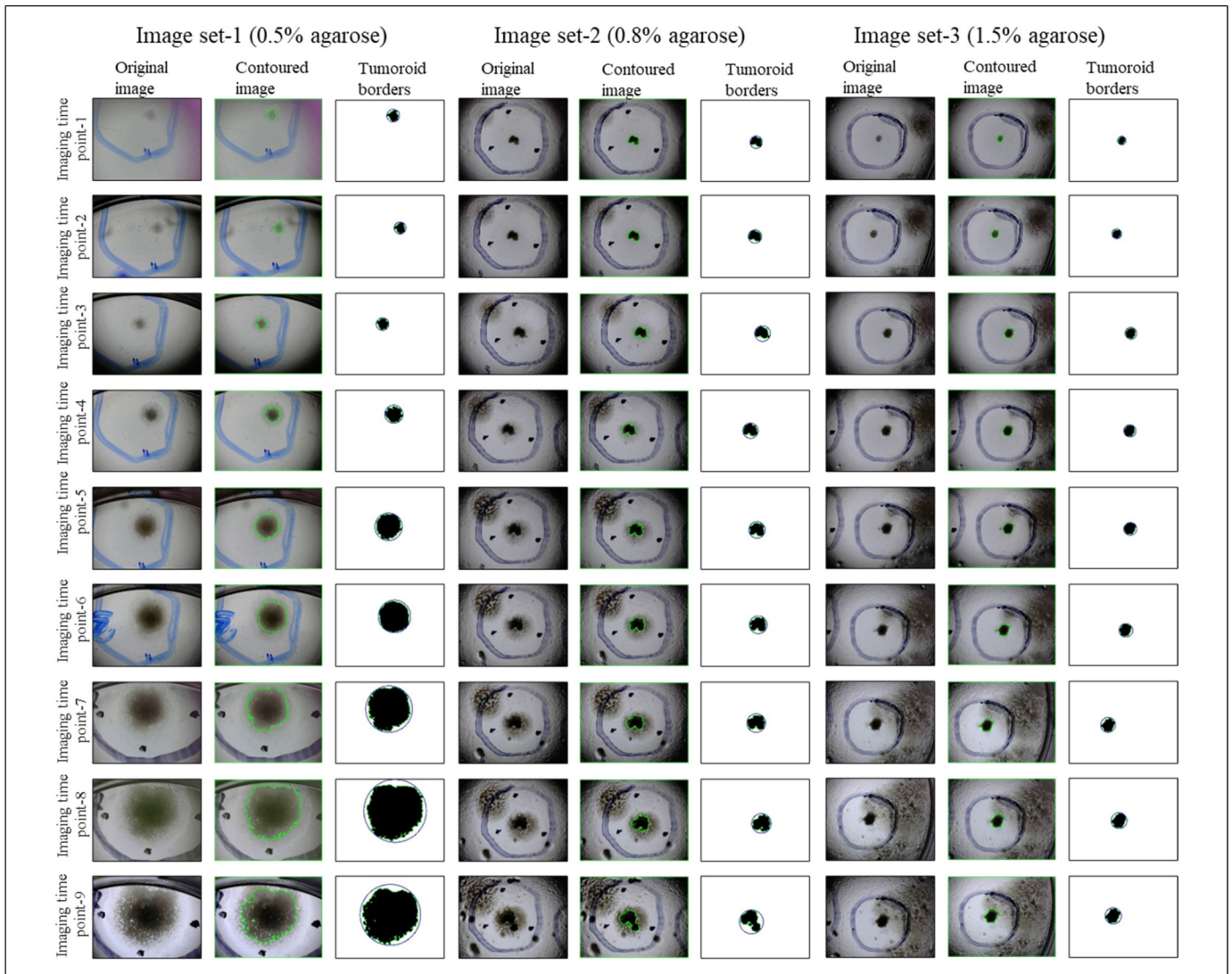
Figure 7. Original, contoured, and binary images for 9 imaging time points of image sets-1, 2, and 3. In binary images, tumoroid borders and minimum enclosing circles tumoroid were drawn automatically. The tumoroids produced with 0.5% agarose concentration (image set-1), 0.8% agarose concentration (image set-2), and 1.5% agarose concentration (image set-3) showed a 33.07-, 4.33-, and 3.80 times growth increase from imaging time point-1 to imaging time point-9, respectively.
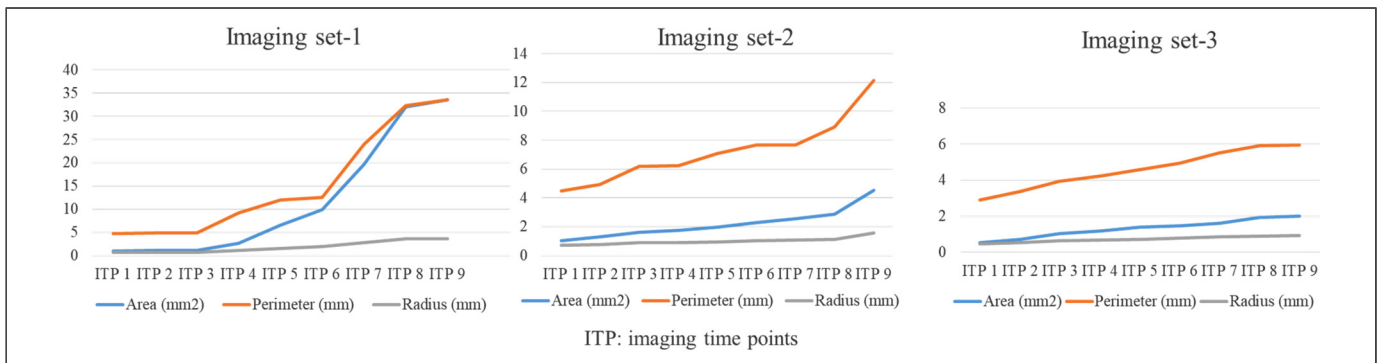

Figure 8. Growth trend of 3 tumoroids with 0.5%, 0.8%, and 1.5% agarose concentrations over time.

Joseph et al.,[39] a K-means clustering algorithm has been proposed for the segmentation of brain MRI images to extract suspicious regions. In our study, we applied the thresholding method including a variety of filtering methods as the segmentation process since we needed to separate 2 main regions, the tumoroid mass and its background.

In a study by Yang et al.,[42] in addition to the importance of the partial clustering method to classify data in a certain group, it is emphasized that as the number of features in the data set increases, more clusters are needed. In our study, we used the global thresholding method in the segmentation stage to classify the pixels containing the tumoroid structure in the images. In the morphological operations that we use to obtain the closest image to the tumoroid structures after the classification process, the size selection of the core matrices (kernels) was of great importance as the importance of the cluster number in the partial clustering method. As stated in a study by Kutbay et al.,[44] adjustable distant fuzzy c-means segmentation and quaternion-based convolution filters and saliency mapping procedures were applied separately to measure carotid artery intima-media thickness on 25 carotid Doppler images, and then the results were evaluated with MSE. In our study, we applied the mean, median, bilateral, and Gaussian filters for improving the quality of images and tested the performance of results by implementing the metrics of MSE, PSNR, and CNR. These are quantitative metrics that measure the target object sharpening performance of various filters applied to images with different noise levels. The high PSNR means high image quality and low image degradation, while MSE value on the same image is expected to be low and having a high CNR means achieving the high distinguishability power of the target object as well.

Cell culture platforms provide excellent preclinical research tools to study diseases such as pancreatic cancer. The computer-aided systems play an important role in the imaging of cell cultures. In this study, we comprehensively investigated the growth characteristic of pancreatic tumoroid produced with MIA PaCa-2 cancer cells by the mini-Opto tomography imaging system that has the ability to image the full size of tumoroids with up to a few cm in size. The 3 tumoroids were cultured in 0.5%, 0.8%, and 1.5% agarose gel, imaged enlarging borders of, and analyzed the growth rate of each at 9 different imaging time points. The image processing techniques such as color transformation, filtering, morphological process, thresholding, contouring, and feature extraction were applied to a total of 27 images of 3 tumoroids (image sets-1, 2, and 3), each with 9 imaging time points. In quantitative evaluation, the median filtering method provided the superior results with the values of PSNR (at each of 9 imaging time points in the range of 46.656 to 57.675 for image set-1, 43.108 to 47.904 for image set-2, and 43.981 to 50.316 for image set-3) and MSE (at each of 9 imaging time points in the range of 0.111 to 1.404 for image set-1, 1.053 to 3.178 for image set-2, and 0.604 to 2.599 for image set-3). In the CNR metric assessment, the bilateral and Gaussian filters gave the highest CNR values (i.e., Gaussian filter: at each of 9 imaging time points in the range of 1.715 to 15.142 for image set-1,

10.779 to 41.716 for image set-2, and 11.974 to 45.302 for image set-3) compared to the CNR values of median-filtered images because the median filter caused smoother images and smoothing produced lower CNR values. As image features of 3 tumoroids, the radius, perimeter, and area of tumoroid with 0.5% agarose concentration were 0.670 mm, 4.758 mm, and 1.014 mm^2 at the imaging time point-1; 3.680 mm, 33.569 mm, and 33.535 mm^2 at the imaging time point-9, which means the tumoroid grew up to 33.07 times in area-size over this period. Similarly, the area of tumoroid with 0.8% agarose concentration was 1.047 mm^2 at the imaging time point-1; 4.538 mm^2 at the imaging time point-9 (indicates 4.33 times growth), the area of tumoroid with 1.5% agarose concentration was 0.530 mm^2 at the imaging time point-1; 2.017 mm^2 at the imaging time point-9 (indicates 3.80 times growth).

The results showed that using the combination of the image processing techniques (with OpenCV tools in Phyton) and the mini-Opto tomography imaging system was useful for observing the changes and growth of a biological sample such as a tumor in the manner of automatically drawing the contours of it and calculating the contour areas of its boundaries. To propose the observation of the tumoroid characterization could assist cancer researchers is one of the critical key points of this study. This study encouraged us to create a mathematical model of the tumor-growing behavior at a time point of imaging and interpreting the growth of the various cancer structures at certain time intervals for our next studies.

Conclusion

The tumoroid cultured with low-concentrated agarose gel grew much faster and the tumoroid growth trend decreased as the agarose concentration was increased in the same time period. A reference circle generated automatically that has a minimum diameter fully surrounding the tumoroid was recommended to predict the future potential borders of the tumoroid. Calculations of area, perimeter, and radius parameters for image sets of 3 different tumoroids gave insight into the growth of the respective tumoroid. Thus, we suggested that these parameters could be used to trace such tumoroids in similar studies. In conclusion, we proposed a system that combines image processing techniques and the mini-Opto tomography imaging platform to trace the 2D growth of tumoroids in a limited time interval and estimate the area these tumoroids would occupy over time.

Declaration of Conflicting Interests

Ethical Approval

Funding

ORCID iD

Adem Polat ![ORCID] https://orcid.org/0000-0002-5662-4141

References

1. Andersen HB, Baden H, Brahe N, Burcharth F. Pancreaticoduodenectomy for periampullary adenocarcinoma. *J Am Coll Surg*. 1994;179(5):545-552.

2. Cheng Y, Wang K, Geng L, et al, Identification of candidate diagnostic and prognostic biomarkers for pancreatic carcinoma. *EBioMedicine*. 2019;40(2019):382–393.

3. Ilic M, Ilic I. Epidemiology of pancreatic cancer. *World J Gastroenterol*. 2016;22(44):9694.

4. Polat A, Göktürk D. An alternative approach to tracing the volumic proliferation development of an entire tumor spheroid in 3D through a mini-Opto tomography platform. *Micron*. 2022;152(2022):103173.

5. Quah S. *International Encyclopedia of Public Health*. Academic Press; 2016.

6. Vincent A, Herman J, Schulick R, Hruban RH, Goggins M. Pancreatic cancer. *The Lancet*. 2011;378(9791):607-620.

7. Ehlen L, Arndt J, Treue D, et al. Novel methods for in vitro modeling of pancreatic cancer reveal important aspects for successful primary cell culture. *BMC cancer*. 2020;20(1):1-13.

8. Kapałczyńska M, Kolenda T, Przybyła W, et al. 2D and 3D cell cultures–a comparison of different types of cancer cell cultures. *Arch Med Sci*. 2018;14(4):910-919.

9. Norberg K, J, Liu X, Fernández Moro C, et al. A novel pancreatic tumour and stellate cell 3D co-culture spheroid model. *BMC cancer*. 2020;20(1):1-13.

10. Kaya M, Stein F, Rouwkema J, Khalil IS, Misra S. Serial imaging of micro-agents and cancer cell spheroids in a microfluidic channel using multicolor fluorescence microscopy. *PLoS One*. 2021;16(6):e0253222.

11. Polat A, Hassan S, Yildirim I, et al. A miniaturized optical tomography platform for volumetric imaging of engineered living systems. *Lab Chip*. 2019;19(4):550-561.

12. Sogomonyan AS, Shipunova VO, Soloviev VD, Larionov VI, Kotelnikova PA, Deyev SM. 3D models of cellular spheroids as a universal tool for studying the cytotoxic properties of anticancer compounds in vitro. *Acta Naturae*. 2022;14(1):92-100.

13. Ginsburg O, Yip CH, Brooks A, et al. Breast cancer early detection: a phased approach to implementation. *Cancer*. 2020;126(S10):2379-2393.

14. Shen Y, Pu K, Zheng K, et al. Differentially expressed microRNAs in MIA PaCa-2 and PANC-1 pancreas ductal adenocarcinoma cell lines are involved in cancer stem cell regulation. *Int J Mol Sci*. 2019;20(18):4473.

15. Cahoon TC, Sutton MA, Bezdek JC. Breast cancer detection using image processing techniques. In: Ninth IEEE International Conference on Fuzzy Systems. FUZZ-IEEE 2000 (Cat. No. 00CH37063), Vol. 2. IEEE, 2000, pp. 973-976.

16. Ramadan SZ. Methods used in computer-aided diagnosis for breast cancer detection using mammograms: a review. *J Healthc Eng*. 2020;2020:1-21.

17. Waghulade KT, Yadav AK. Early breast cancer detection by using image processing. In: International Conference on Innovative Trends in Engineering Research (ICITER-2016), 2016, pp. 147-151.

18. Polat A, Matela N, Dinler A, Zhang YS, Yildirim I. Digital breast tomosynthesis imaging using compressed sensing based reconstruction for 10 radiation doses real data. *Biomedical Signal Processing Control*. 2019;48(2019):26-34.

19. Alhadidi B, Zu'bi MH, Suleiman HN. Mammogram breast cancer image detection using image processing functions. *Inf Technol J*. 2007;6(2):217-221.

20. Bankhead P, Loughrey MB, Fernández JA, et al. Qupath: open source software for digital pathology image analysis. *Sci Rep*. 2017;7(1):1-7.

21. Culjak I, Abram D, Pribanic T, Dzapo H, Cifrek M. A brief introduction to OpenCV. In: 2012 Proceedings of the 35th International Convention MIPRO, Opatija, Croatia. IEEE, 2012, pp. 1725-1730.

22. Li S, Qin B, Xiao J, Liu Q, Wang Y, Liang D. Multi-channel and multi-model-based autoencoding prior for grayscale image restoration. *IEEE Trans Image Process*. 2019;29:142-156.

23. Reddy RVK, Raju KP, Kumar LR, Kumar MJ. Grey level to RGB using YCbCr color space technique. *Int J Comput Appl*. 2016;147(7):25-28.

24. Xie G, Lu W. Image edge detection based on opencv. *International Journal of Electronics Electrical Engineering*. 2013;1(2):104-106.

25. Raman S, Chaudhuri S. Bilateral filter based compositing for variable exposure photography. In: Eurographics (Short Papers), 2009, pp. 1-4.

26. Akar E, Kara S, Akdemir H, Kırış A. A MATLAB tool for an easy application and comparison of image denoising methods. In: 2015 Medical Technologies National Conference (TIPTEKNO). IEEE, 2015, pp. 1-4.

27. Banterle F, Corsini M, Cignoni P, Scopigno R. A low-memory, straightforward and fast bilateral filter through subsampling in spatial domain. *Computer Graphics Forum*. 2012;31(1):19-32.

28. Tomasi C, Manduchi R. Bilateral filtering for gray and color images. In: Sixth International Conference on Computer Vision (IEEE Cat. No. 98CH36271). IEEE, 1998, pp. 839-846.

29. Gonzalez RC, Woods RE. *Digital Image Processing*. Addison-Wesley; 1992.

30. Polat A, Yildirim I. An iterative reconstruction algorithm for digital breast tomosynthesis imaging using real data at three radiation doses. *Journal of x-ray Science Technology*. 2018;26(3):347-360.

31. Vij K, Singh Y. Enhancement of images using histogram processing techniques. *Int J Comp Tech Appl*. 2009;2(2):309-313.

32. Karaca N. Alçak Çözünürlüklü Fotoğrafların Görüntülenmesi ve Bunların Optimizasyonu İle İlgili Bir Çalışma / A study of rendering low resolution images and optimization of these low resolution images. Ege University; 2007

33. Liu N, Zhai G. Free energy adjusted peak signal to noise ratio (FEA-PSNR) for image quality assessment. *Sensing Imaging*. 2017;18(1):1-10.

34. Takaoğlu F. DWT ve DCT steganografide performans analizi / Performance Analysis of DWT and DCT on Steganography. İstanbul Aydın University; 2016

35. Boateng KO, Asubam BW, Laar DS. Improving the effectiveness of the median filter. *International Journal of Electronics Communication Engineering*. 2012;5(1):85-97.

36. Senthilkumaran N, Vaithegi S. Image segmentation by using thresholding techniques for medical images. *Computer Science Engineering: An International Journal*. 2016;6(1):1-13.

37. Borole VY, Nimbhore SS, Kawthekar SS. Image processing techniques for brain tumor detection: A review. *International Journal of Emerging Trends Technology in Computer Science*. 2015; 4(2):1-14.

38. Wang Q, Gui N, Liu Y, et al. A morphological image processing method for simultaneous scrutinization of particle position and velocity in pebble flow. *Ann Nucl Energy*. 2020;148(2020): 107704.

39. Joseph RP, Singh CS, Manikandan M. Brain tumor MRI image segmentation and detection in image processing. *International Journal of Research in Engineering Technology*. 2014;3(1):1-5.

40. McAndrew A. *An Introduction to Digital Image Processing With MATLAB Notes for scm2511 Image Processing I, School of Computer Science and Mathematics, Victoria University of Technology*. Course Technology Press, Boston; 2004.

41. Tiu G. Classification of drill core textures for process simulation in geometallurgy. Luleå University of Technology; 2017.

42. Yang S, Jiang Z, Pan W. Egg image feature value extraction method based on openCV+python. International Conference on Computer Intelligent Systems and Network Remote Control (CISNRC 2019).2019.

43. Al-Shamlan H, El-Zaart A. Feature extraction values for breast cancer mammography images. In: 2010 International Conference on Bioinformatics and Biomedical Technology. IEEE, 2010, pp. 335-340.

44. Kutbay U, Hardalaç F, Akbulut M, Akaslan Ü, Serhatlıoğlu S. A computer-aided diagnosis system for measuring carotid artery intima-media thickness (IMT) using quaternion vectors. *J Med Syst*. 2016;40(6):1-12.